

Algorithm for Flat First-Year Ice Draft Using AMSR2 Data in the Arctic Ocean

E. YOSHIKAWA

Division of Polar Ocean Sciences, Korea Polar Research Institute, Incheon, South Korea

K. SHIMADA

Department of Ocean Sciences, Tokyo University of Marine Science and Technology, Tokyo, Japan

K. H. CHO

Division of Polar Ocean Sciences, Korea Polar Research Institute, Incheon, South Korea

(Manuscript received 12 March 2018, in final form 9 September 2018)

ABSTRACT

First-year ice has replaced multiyear ice in the Northern Sea Route area since 2008. In this area, sea ice survival during summer substantially depends on first-year ice thickness at melt onset, and thus monitoring of first-year ice thickness in the freezing period is a key to forecasting sea ice distributions in the following summer. In this paper we introduce a new algorithm to estimate flat first-year ice draft using brightness temperature data measured by the Advanced Microwave Scanning Radiometer-2 (AMSR2). The algorithm uses a gradient ratio (GR) of 18- and 36-GHz vertically polarized brightness temperatures based on decreases in sea ice emissivity in higher AMSR2 frequency channels with thermodynamic growth associated with an increase in volume scattering. Such spectral characteristics of the emissivity are examined by comparing GR values with flat first-year ice draft extracted by mode values of in situ draft data measured by a moored ice profiling sonar. The accuracy of the daily draft estimated from GR values after applying proper noise filters is about 10 cm for a draft range of 0.4–1.2 m.

1. Introduction

The ice-free duration has lengthened in Arctic marginal seas (such as the Chukchi, East Siberian, and Laptev Seas), corresponding to the Northern Sea Route area during the last decade (Markus et al. 2009; Stroeve et al. 2014). The lengthening increases potential opportunities for Arctic shipping, and there are growing demands for forecasts of summer sea ice distributions associated with route availability. In addition to weather conditions and sea ice movements during summer, sea ice thickness at melt onset is one of the important factors affecting sea ice survival through summer. The ice thickness in the Northern Sea Route area, where most of the multiyear ice (MYI) has been replaced by first-year ice (FYI) since 2008 (Maslanik et al. 2011; Comiso 2012), is determined by FYI growth in the preceding freezing period. Therefore, monitoring of FYI thickness is crucially important for forecasting sea ice distributions in the following summer.

Variations in FYI thickness at melt onset range within 1–2 m depending on its growth in the freezing period. To detect such variations, thickness data with an accuracy of 10–20 cm are required. Currently, altimetry-derived thickness data are available based on satellite freeboard measurements (Kwok et al. 2009; Laxon et al. 2013), but they are not accurate enough to detect the FYI thickness variations (Tilling et al. 2015). Moreover, altimeters take about one month to map thickness data across the entire Arctic Ocean. Sea ice thickness can also be estimated using brightness temperature data measured by satellite passive microwave radiometers, such as the Advanced Microwave Scanning Radiometer-2 (AMSR2), based on an empirical relation between emissivity and sea ice thickness. Unlike the altimetry method, this microwave method enables us to monitor sea ice thickness in near-real time. To date, the thickness algorithm has been well established for thin ice using a polarization ratio (PR) of brightness temperature data between horizontal and vertical polarizations (Martin et al. 2004; Tamura and Ohshima 2011; Iwamoto et al. 2014).

Corresponding author: Eri Yoshizawa, yoshizawa@kopri.re.kr

DOI: 10.1175/JTECH-D-18-0034.1

© 2018 American Meteorological Society. For information regarding reuse of this content and general copyright information, consult the [AMS Copyright Policy](https://www.ametsoc.org/PUBSReuseLicenses) (www.ametsoc.org/PUBSReuseLicenses).

On the other hand, the algorithm for relatively thicker ice without discriminating between FYI and MYI was proposed using a gradient ratio (GR) of 6- and 36-GHz brightness temperature data in the vertical polarization (Krishfield et al. 2014), but estimated results with 60-cm errors are not accurate enough for detecting the FYI thickness variations. This algorithm is based on a relation between the GR and daily mean sea ice draft measured using a moored ice profiling sonar (IPS), for which both flat and rafted/ridged sea ice are involved. Thermodynamic growth decreases brine volume in sea ice, resulting in increases in volume scattering and thus decreases in microwave emissivity in high-frequency channels. Mechanical growth, however, does not result in such changes; that is, it is uncorrelated with the emissivity changes. This suggests that the thickness algorithm for thicker ice should be developed using the following four parts. The first part is to develop an algorithm for flat FYI thickness based on the emissivity changes. The second part is to develop an algorithm for amplifications of flat FYI thickness caused by mechanical rafting/ridging using high-accuracy sea ice motion data. The third part is integrations of the two algorithms for FYI. The fourth part is coupling with altimetry-derived thickness of MYI.

The present study is identified as the first part, development of flat FYI monitoring using passive microwave data. We attempt to present an algorithm to estimate flat FYI draft using AMSR2 brightness temperature data. For this purpose, we significantly improve the accuracy of reference data—that is, in situ IPS-measured draft data—and identify flat sea ice draft for comparison with brightness temperature data. Since some microwave frequency channels are sensitive to not only volume scattering from sea ice but also atmospheric water vapor and cloud liquid water (Gloersen and Cavalieri 1986) as well as volume scattering from snow cover on sea ice (Comiso et al. 1989; Markus and Cavalieri 1998), we also address noise filters for brightness temperature data. Based on these processes, we will demonstrate the potential of the microwave method to provide draft estimates with sufficient accuracy for detecting FYI growth in the freezing period. As described earlier, the algorithm is based on an empirical relationship between sea ice emissivity and thickness. Because this relationship associated with winter thermodynamic growth would be modified when sea ice surface melting occurs, the algorithm can be applied only for the freezing period. To bridge gaps between the empirical thickness estimation and theoretical model of the microwave scattering, it is important to identify which physical or structural properties of sea ice result in changes in microwave emissivity. However, further in situ measurements or laboratory

experiments are required to resolve this issue. Therefore, a full analysis of the sea ice properties that correlate with the emissivity changes is beyond the scope of this paper.

This paper is organized as follows. Section 2 introduces the satellite and in situ data. Section 3 examines the emissivity changes dependent on the identified flat sea ice draft in order to present the draft algorithm for flat ice. The presented algorithm is applied to mapping. Section 4 provides a summary and discussion of future work for further developments of the thickness monitoring.

2. Data

a. AMSR2-derived data

The AMSR2 aboard the *Global Change Observation Mission–Water (GCOM-W)* has obtained brightness temperature data using horizontally and vertically polarized channels with multiple frequencies since 2012. We analyze daily averages of the vertically polarized brightness temperature data at 6.9, 10.7, 18.7, 23.8, 36.5, and 89.0 GHz gridded on 10×10 -km² polar stereographic grids, from AMSR2 level 3 (L3) products provided by the Japan Aerospace Exploration Agency (JAXA; <https://gportal.jaxa.jp>). Data from October 2014 to August 2015 are analyzed. We further select data from November to February to present a draft algorithm. In this period, influences of surface melt of sea ice on brightness temperature data can be ignored, because surface air temperatures from the National Centers for Environmental Prediction–National Center for Atmospheric Research (NCEP–NCAR) reanalysis dataset (Kalnay et al. 1996; provided at <http://www.esrl.noaa.gov/psd>) were consistently below -10°C in the Arctic Ocean. We adopt the daily averages composed of data measured in descending scenes. Sea ice concentration (SIC) data from the L3 products are also used.

b. In situ data

We use in situ data measured using an IPS mounted on an ocean mooring deployed at 77°N , 170°E in the Chukchi Abyssal Plain (Fig. 1), located in the western Canada basin (provided at <https://ads.nipr.ac.jp/dataset/A20140425-003>). The observational period of this mooring was October 2014–August 2015. The IPS was mounted to the top of the mooring line, and its instrument depth was approximately 22.5 m. The sampling intervals for the IPS measurements were 1 s for acoustic ranging data and 10 s for pressure and instrument tilt data. The pressure and tilt data are interpolated to 1-s intervals for joint use with the ranging data.

Figure 2 is a schematic showing the IPS measurements to obtain sea ice draft. The IPS provides distance r from

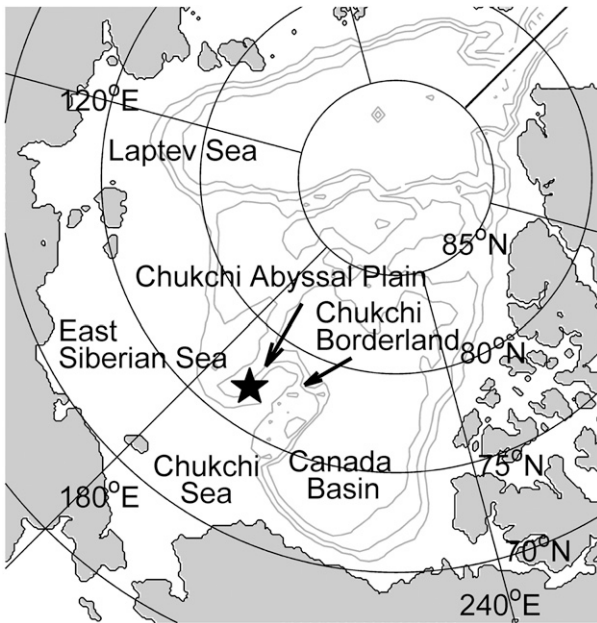


FIG. 1. Map of the study region with depth contours of seafloor topographies at depth intervals of 1000 m. The location of the ocean mooring (77°N, 170°E) is indicated by the star.

its sensor to the sea ice bottom by measuring sound wave travel times. Because the travel times are calculated using a fixed sound speed of 1450 m s^{-1} , the distance data contain errors arising from actual sound speed variations. Thus, sea ice draft η is obtained by subtracting the corrected r from the IPS instrument depth D ,

$$\eta = D - \beta r \cos \theta, \quad (1)$$

where β represents the ratio of actual sound speeds to the fixed sound speed, and θ is the IPS instrument tilt. The instrument depth D is calculated by

$$g \int_{-D}^0 \rho dz = P_{\text{IPS}} - P_{\text{atm}}, \quad (2)$$

where g is the gravitational acceleration calculated for each depth using the latitude at the mooring site, ρ is in situ density of seawater, and P_{IPS} is pressure at the instrument depth caused by seawater and atmospheric loading measured by the IPS. Atmospheric pressure at sea level P_{atm} is determined from sea level pressure data from the NCEP–NCAR reanalysis dataset. In this study, a bias in the reanalysis sea level pressure data relative to actual pressure data is estimated by comparing the reanalysis pressure data with the following two pressure datasets: atmospheric pressure data measured by the IPS maintained on the deck of the South Korean icebreaker *ARAON* for about one week after the recovery of the ocean mooring and shipboard

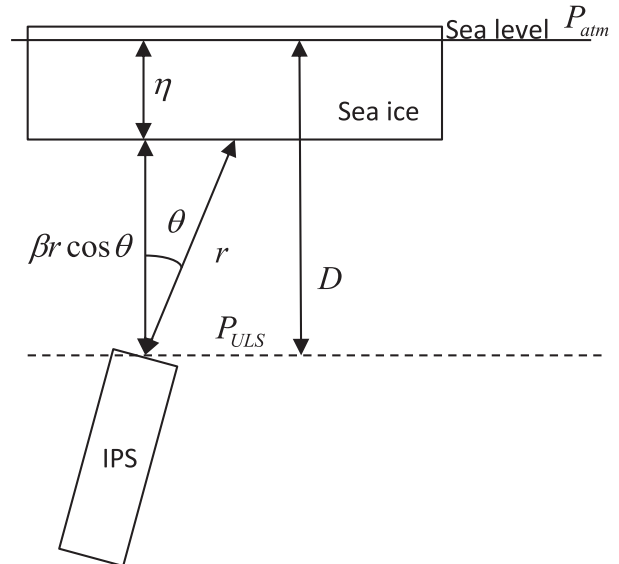


FIG. 2. Schematic showing IPS measurements used to calculate sea ice draft.

atmospheric pressure data measured by the *ARAON* during the Arctic research cruise. From the comparisons, the bias is estimated to be about 3.3 hPa. The standard deviation of the differences between the reanalysis pressure data after the removal of the bias and the IPS pressure data is about 0.6 hPa.

Errors in the IPS-measured draft are mainly attributed to variations in actual sound speeds. We calculate the sound speeds using hydrographic data measured by a conductivity–temperature–depth (CTD) sensor moored below the IPS. The instrument depth of this moored CTD sensor was approximately 25 m, which nearly corresponds to the boundary between the surface mixed layer and the underlying Pacific Summer Water (PSW) layer. Therefore, the actual sound speeds are accurately determined using only moored CTD records, when the CTD sensor was within the surface mixed layer where hydrographic properties and thus sound speeds are vertically homogeneous. Figure 3 shows monthly scatterplots of potential temperature versus salinity (T – S) obtained from the moored CTD records. The monthly T – S properties (black points) in November–February are almost the same as those in the surface mixed layer indicated by freezing temperatures (black lines), whereas the properties are warmer and more saline in other months, suggesting the influences of PSW. This indicates that the CTD sensor was located within the surface mixed layer in November–February. For an accurate validation of a satellite-derived algorithm, we finally select in situ data in the period from November to mid-February, because discrepancies between potential temperatures and freezing temperatures become large

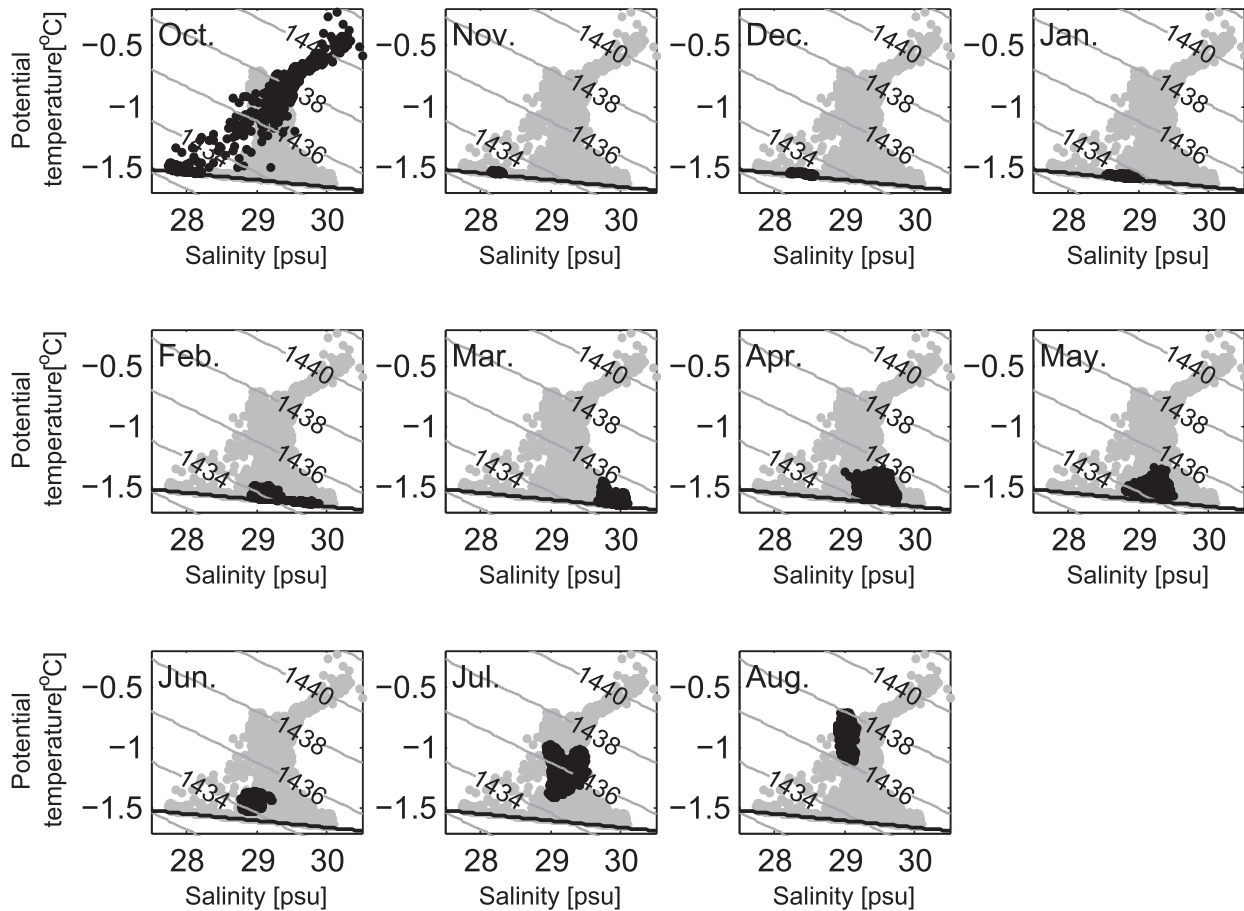


FIG. 3. Monthly scatterplots of potential temperature vs salinity obtained from moored CTD observations at approximately 25 m. Data in each month are plotted using black points, and all available data in October–August are plotted using gray points. Black lines represent freezing temperatures. Gray contours are isolines of sound speeds.

in late February. The mean value of the sound speeds for that period is $1433.5 \pm 0.3 \text{ m s}^{-1}$. Consequently, errors of the IPS-measured draft data used in this study are estimated to be less than 3 cm, showing significant improvements in accuracy compared to data with 10-cm errors used to date (Krishfield et al. 2014).

An upward acoustic Doppler current profiler (ADCP) was also installed on the mooring. According to the ADCP measurements, the mean absolute sea ice velocity is about 9.8 km day^{-1} for November–February. This indicates that daily statistics of the IPS-measured draft data reflect information on sea ice distributed in a 10-km area around the mooring site as a result of sea ice motions. In the next section, we therefore compare the daily statistics with daily averaged brightness temperature data at the AMSR2 grid cell nearest to the mooring site. The daily statistics are calculated from draft samples collected within $\pm 12 \text{ h}$ relative to the mean observational time of brightness temperature data at the AMSR2 grid cell.

3. Algorithm for flat FYI draft

a. Identification of flat sea ice draft

To present a draft algorithm for flat FYI, we first consider which daily statistics of IPS-measured draft can identify flat sea ice draft. Because the areal extents of flat ice portions are larger than those of rafted/ridged portions in actual ice fields, we expect that flat ice draft can be identified by mode values represented by the first modes in draft probability distributions. In fact, comparing sea ice bottom topographies revealed by the IPS-measured draft recorded at 1-s intervals (gray points in Fig. 4) with a daily mode value (solid line) confirms that most of the draft data are concentrated at the daily mode value of about 0.7 m, thus showing flat bottom topographies. Such features are seen in other daily segments of the IPS-measured draft (not shown). In contrast to the flat sea ice, keels of rafted/ridged ice appear less frequently, so the rafted/ridged ice does not cause prominent modes in draft probability distributions and thus does not contribute to

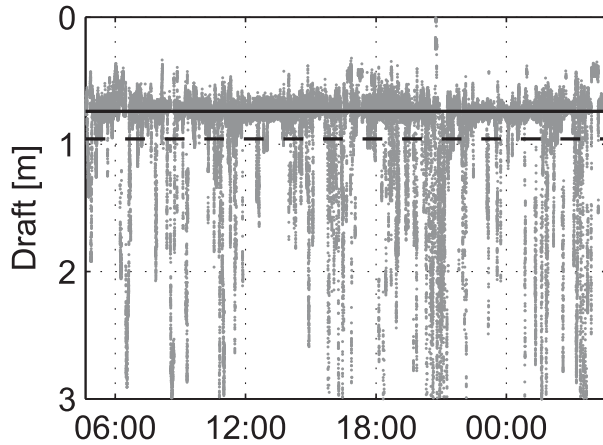


FIG. 4. Time series of IPS-measured draft recorded at 1-s intervals (gray points) compared with the daily mode and mean draft (solid and dashed lines, respectively) on 16 Dec 2014.

the mode draft. On the other hand, their presence causes the mean draft value (dashed line) to be about 0.3 m larger than the daily mode value. The results show that the use of the mode draft enables us to identify flat sea ice draft and to rule out effects of rafted/ridged ice.

The draft probability distributions, however, occasionally exhibit multiple sea ice modes as seen in monthly distributions (Fig. 5). For example, the distributions in December show a multimodal structure with one mode centered around 0.7 m and the other centered around 1.0 m (red line). Such multiple modes appear in the distributions when younger flat ice formed in lead areas was observed in addition to relatively older flat ice. To eliminate cases showing the multiple sea ice modes, we calculate moments of daily draft probability distributions around daily mode values. If the moment normalized by the daily mode draft exceeds 0.6, then we do not use the daily mode draft values for algorithm validations. This filtering process eliminates data corresponding to about 25% of the time series (data in shaded regions in Fig. 6).

The filtered daily mode draft increases from 0.4 to 1.2 m, corresponding to the earlier growth stage of FYI from November to mid-February (black line in Fig. 6). The mean draft also shows seasonal evolutions (gray line), but it is consistently larger than the mode draft, suggesting the presence of rafted/ridged ice throughout the period. Therefore, changes in sea ice emissivity depending on flat sea ice draft will be examined by comparing in situ mode draft values with brightness temperature data. Before doing so, we next address noise filtering for brightness temperature data.

b. Noise filters for brightness temperature data

We here attempt to choose brightness temperature data that are affected only by volume scattering of

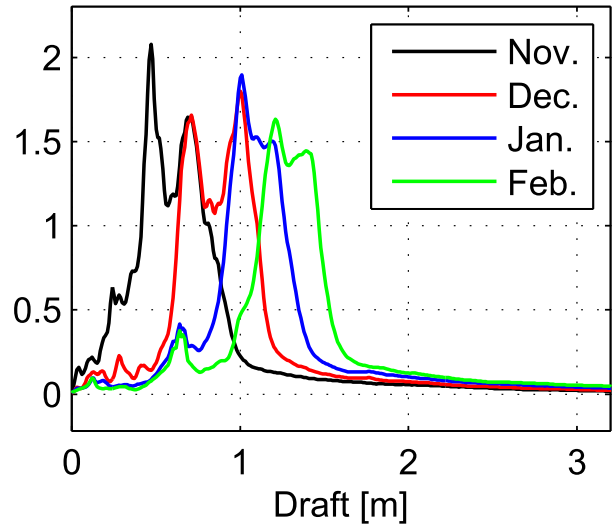


FIG. 5. Monthly draft probability distributions binned into 1-cm intervals in November–February.

FYI using the following two parameters introduced by Cavalieri et al. (1984):

$$\text{PR}(\nu) = [T_B(\nu V) - T_B(\nu H)] / [T_B(\nu V) + T_B(\nu H)] \quad (3)$$

and

$$\text{GR}(\nu_1 V, \nu_2 V) = (T_B \nu_1 V - T_B \nu_2 V) / (T_B \nu_1 V + T_B \nu_2 V), \quad (4)$$

where T_B is brightness temperature. PR is a measure of the polarization differences between horizontally (H) and vertically (V) polarized brightness temperature data at a single frequency ν . Thin ice and open water are identified by PR values larger than those of thicker ice such as FYI and MYI (Cavalieri 1994). On the other hand, GR represents spectral gradients of brightness temperature data between two different frequencies (ν_1 and ν_2). The combination of 18- and 36-GHz data in a vertical polarization is utilized to discriminate FYI from MYI. The combined use of the two parameters identifies a dominant sea ice type in observational fields. Figure 7a shows a scatterplot of PR(18) versus GR(18V, 36V) around the mooring site from October 2014 to August 2015. In this figure, as the PR–GR plot migrates toward tie points for MYI, FYI, and open water (red points), fractions of each sea ice type are increased. Although the PR–GR plot more closely approaches the tie points for MYI and open water in some cases, most of the points are clustered around the tie point for FYI, especially in the period from November to mid-February (black points). This is interpreted as high FYI

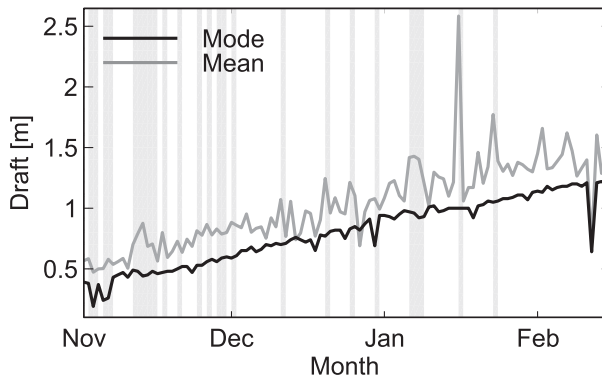


FIG. 6. Time series of daily mode and mean draft values (black and gray lines, respectively). The gray shaded regions indicate times with daily draft probability distributions showing multiple sea ice modes. The multiple sea ice modes are identified by normalized moments of the draft probability distributions above 0.6.

fractions and agrees with in situ IPS measurements consistently showing FYI draft in the same period. The cluster of points around the FYI tie point, enlarged in Fig. 7b, shows that GR values continuously vary in direction from the FYI tie point to the MYI tie point. This is a result of seasonal increasing in the GR values (Fig. 8a), which resembles flat FYI growth extracted by temporal variations in mode draft values (Fig. 6). The time series of the GR values, however, shows a higher temporal variability compared with that of in situ flat ice draft, likely caused by contamination effects on brightness temperature data. These results suggest that the spectral gradients of brightness temperature data after filtering out the contamination effects can be used to detect draft variations of flat FYI.

The PR–GR plot shows dispersions in the direction of the PR axis (black points in Fig. 7b). This is considered

to be related to the following polarization characteristics of brightness temperature data—the polarization differences tend to decrease (increase) as a result of the scattering effects of a medium with randomly (preferentially) oriented particles or microstructures. For instance, water vapor, cloud liquid water, and new snow cause the former type of scattering, and thin ice and open water are associated with the latter. Based on these polarization characteristics, we attempt to filter out noises in brightness temperature data. Here we adopt PR values of 36- and 89-GHz data instead of 18-GHz data, because microwave channels are more affected by snow scattering with increasing frequencies (e.g., Comiso et al. 1989). The use of the 89-GHz data is also effective for ruling out weather-related contaminations, because the data show a pronounced sensitivity to atmospheric scattering. At the mooring site, both PR(36) and PR(89) values occasionally exhibit rapid decreases, suggesting the snow or atmospheric scattering effects (Fig. 8b). On the other hand, the PR(36) values anomalously increase in mid-November, when ice openings tend to occur (Kwok 2006). Because such large PR values greater than about 0.040 coincide with values for thin ice in Arctic polynyas (Iwamoto et al. 2014), we assume that thin ice formations caused by ice opening events act as noise in brightness temperature data in this period. From these temporal variations in the PR values, we set maximum and minimum thresholds for the PR values summarized in Table 1 as noise filters. These noise filters identify brightness temperature data as contaminant data when the PR values are in shaded regions in Fig. 8b. Although a minimum threshold for SIC is also set to identify open water contaminations, the contaminations are negligibly small.

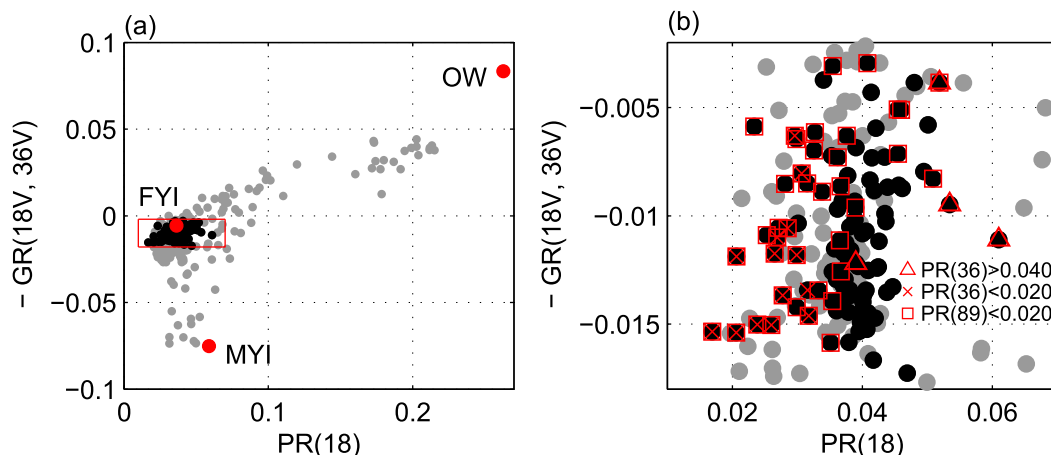


FIG. 7. (a), (b) Scatterplots of PR(18) vs GR(18V, 36V). Tie points for MYI, FYI, and open water are indicated by red points in (a). The area within the red box in (a) is enlarged in (b). Points with red triangles, crosses, and squares indicate contaminated data identified by the maximum and minimum thresholds of PR(36) and the minimum threshold of PR(89) listed in Table 1, respectively.

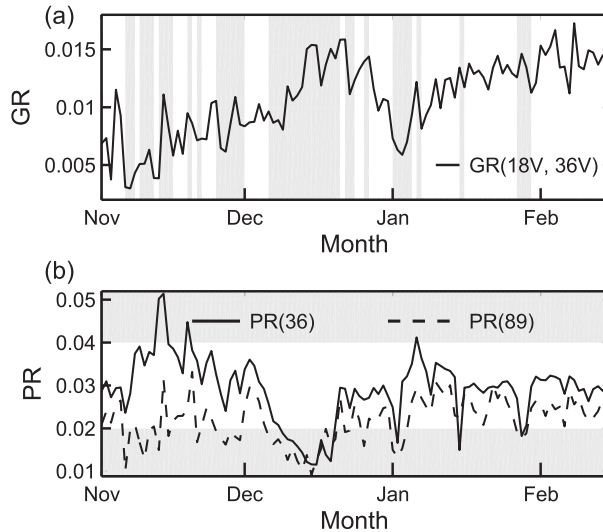


FIG. 8. (a) Time series of GR(18V, 36V) at the mooring site. The gray shaded regions indicate times with contamination effects in brightness temperature data identified by the maximum and minimum thresholds of PR values listed in Table 1. (b) Time series of PR(36) and PR(89) shown by solid and dashed lines, respectively. PR values in the gray shaded regions are above (below) the maximum (minimum) threshold.

Among the noise filters, the filter using lower PR(89) values eliminates larger fractions of data compared with other filters (Table 1). The points of the eliminated data are randomly distributed in Fig. 7b (red squares), but they partially coincide with those eliminated by lower PR(36) values (red crosses). The points identified by the two filters seem to spread parallel to the GR axis rather than randomly (overlapped red squares and crosses). Unlike atmospheric scattering effects, the snow scattering effects reduce emissivities in higher-frequency channels with increasing snow depth such that the snow depth is correlated with GR values (e.g., Markus and Cavalieri 1998). Thus, the nearly vertical distributions of the points are considered to represent snow-covered FYI. By filtering out all contaminated data, the dispersions on the PR-GR plot are effectively reduced (black points without red symbols in Fig. 7b), suggesting that the adopted filters are proper. In total, about 40% of the data are judged to be contaminated data in the time series from November to mid-February using all the filters. Next, changes in sea ice emissivity depending on in situ IPS-measured draft are examined using the filtered data.

c. Spectral characteristics of sea ice emissivity depending on flat FYI draft

As described in the preceding subsection, spectral gradients between 18- and 36-GHz data show temporal variations similar to seasonal evolutions in flat FYI,

TABLE 1. Maximum and minimum thresholds of PR(36), PR(89), and SIC set as noise filters for brightness temperature data. The noise filters are intended for scattering effects described in parentheses. The fractions of contaminant data identified by the filters in the time series from November to mid-February are also listed in the parentheses.

	Max threshold	Min threshold
PR(36)	0.040 (thin ice, 4%)	0.020 (snow, 13%)
PR(89)	—	0.020 (snow and atmosphere, 36%)
SIC (%)	—	95 (open water, 1%)

suggesting that sea ice emissivities at higher frequencies above 18 GHz are reduced with FYI growth. To understand such spectral characteristics of sea ice emissivity, we examine dependencies of sea ice emissivities at each frequency on in situ mode draft values using filtered brightness temperature data. For microwave channels, sea ice emissivity ε can be simplified using brightness temperature as follows:

$$\varepsilon = T_B/T_i, \quad (5)$$

where T_i is physical temperature at the interface between ice and snow (Comiso 1983). In this study, we assume that filtered brightness temperature data are affected by only volume scattering of sea ice without snow cover. On the basis of this assumption, T_i is given by physical sea ice temperature at the ice surface. Because of the lack of in situ sea ice temperature data, the present study uses skin temperatures from the NCEP–NCAR reanalysis dataset instead.

To examine emissivity changes dependent on flat FYI draft, the emissivities at each frequency are binned into three values of the daily mode draft, 0.6 ± 0.15 , 0.9 ± 0.15 , and 1.2 ± 0.15 m. The binned emissivities at each frequency are normalized by that at 18 GHz to show spectral gradients among 18 GHz and other frequencies. The normalized values represent relative emissivities in a case in which the emissivity at 18 GHz is set to unity. Figure 9 shows the relative emissivities plotted versus AMSR2 frequencies. In this figure, the emissivity changes at each frequency represent their dependencies on the mode draft values. The relative emissivities at frequencies above 18 GHz decrease as the mode draft values increase, and decline rates become larger with increasing frequencies. Furthermore, the emissivities in a band of 23–89 GHz are smaller than that at 18 GHz for all three mode draft values. This indicates that spectral gradients of the emissivities between 18 GHz and higher frequencies become steep with increasing flat FYI draft and thus offer support that GR values can be used to detect flat draft variations in the earlier growth stage of FYI. From these results, it is expected that the

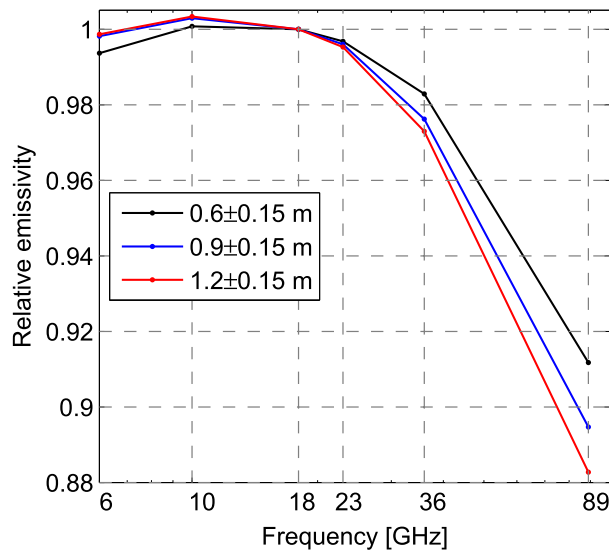


FIG. 9. Relative emissivities calculated from filtered brightness temperature data in vertical polarizations plotted vs AMSR2 frequencies. The emissivities at each frequency are binned into three values of the daily mode draft, 0.6 ± 0.15 , 0.9 ± 0.15 , and 1.2 ± 0.15 m (black, blue, and red lines, respectively). See the text for a further description of the relative emissivities.

combination of 18 and 89 GHz is most suitable for draft estimations, but the 89-GHz data are significantly influenced by weather-related contaminations. Therefore, we adopt the combination of 18- and 36-GHz data in the vertical polarization for an algorithm for flat FYI draft.

d. Algorithm

We derive a draft algorithm by comparing GR with in situ mode draft. Figure 10a shows a scatterplot of unfiltered GR(18V, 36V) versus in situ mode draft. As expected, the GR values at the mooring site increase with increasing mode draft, but they show dispersions caused by the presence of contaminant data denoted by black symbols. After filtering out these contaminant data (Fig. 10b), the draft algorithm for flat FYI is obtained as a linear regression between filtered GR and mode draft:

$$h = aGR + b, \quad (6)$$

where h is flat sea ice draft (m), and $a = 71.5$ and $b = 0.112$ are coefficients calculated from the linear regression. The minimum (maximum) draft that can be estimated by Eq. (6) is set to 0.4 (1.2) m depending on the range of in situ IPS-measured data used for the algorithm validation. The linear fitting is shown by the thick line (Fig. 10b). The adjacent thin lines mark about 15-cm differences, corresponding to 1.5 standard deviations of differences of the plotted points from the

fitted line. The linear regression is derived from data at the points located within the 15-cm difference area (gray points edged with black lines). For the draft range of 0.4–1.2 m, observed and estimated values are closely correlated with each other ($N = 37$, $R = 0.89$). The standard deviation of the differences of the estimated values from the observed values is about 10 cm, indicating that the new algorithm provides draft estimates with accuracy sufficient to detect FYI draft variations.

Figure 11 compares time series of the in situ mode draft (circles) with that of the estimated draft calculated from Eq. (6) using filtered GR values (crosses). Because noise filters eliminate GR values, which exhibit sudden decreases or increases in the shaded regions in Fig. 8a, the estimated draft values show seasonal evolutions similar to the flat FYI growth seen in Fig. 6. At daily temporal resolutions, the draft estimates are partially missing because of contaminations in brightness temperature data. In particular, the estimated results are continuously missing for about 2 weeks in December, likely because of snow or atmospheric scattering effects as identified by low PR values (Fig. 8b). This means that our draft algorithm can provide spatial maps of the draft estimates, with temporal resolutions corresponding to the times required to filter out these scattering effects from brightness temperature data.

e. Application to mapping

Because weather-related contaminations detected by 89-GHz data are most evident among several contamination sources (Table 1), it is expected that our algorithm provides spatial maps of draft estimates with temporal resolutions at least corresponding to the cycles of atmospheric disturbances. To evaluate the performance of our algorithm for mapping, we created spatial maps of weekly averaged draft estimates for January 2017. (Fig. 12). The draft estimates were calculated from Eq. (6) using filtered GR values and are provided up to 2.0 m by extending our algorithm to a thicker FYI range. Areas with estimated values greater than 2.0 m are assumed to be MYI areas that are beyond the scope of our estimation. A discussion about extending our algorithm to the thicker FYI range is given later, and we focus on only influences of the noise filtering processes for brightness temperature data on the mapping performance. The averaged draft estimates are mapped onto most of the areas at weekly temporal resolutions, except for the area adjacent to the Greenland and Canadian Archipelago where MYI consistently exists. This indicates that our algorithm is capable of providing spatial distributions of flat FYI draft with at least weekly temporal resolutions.

In January 2017, areas south of about 77°N in the Pacific sector of the Arctic Ocean, which correspond to

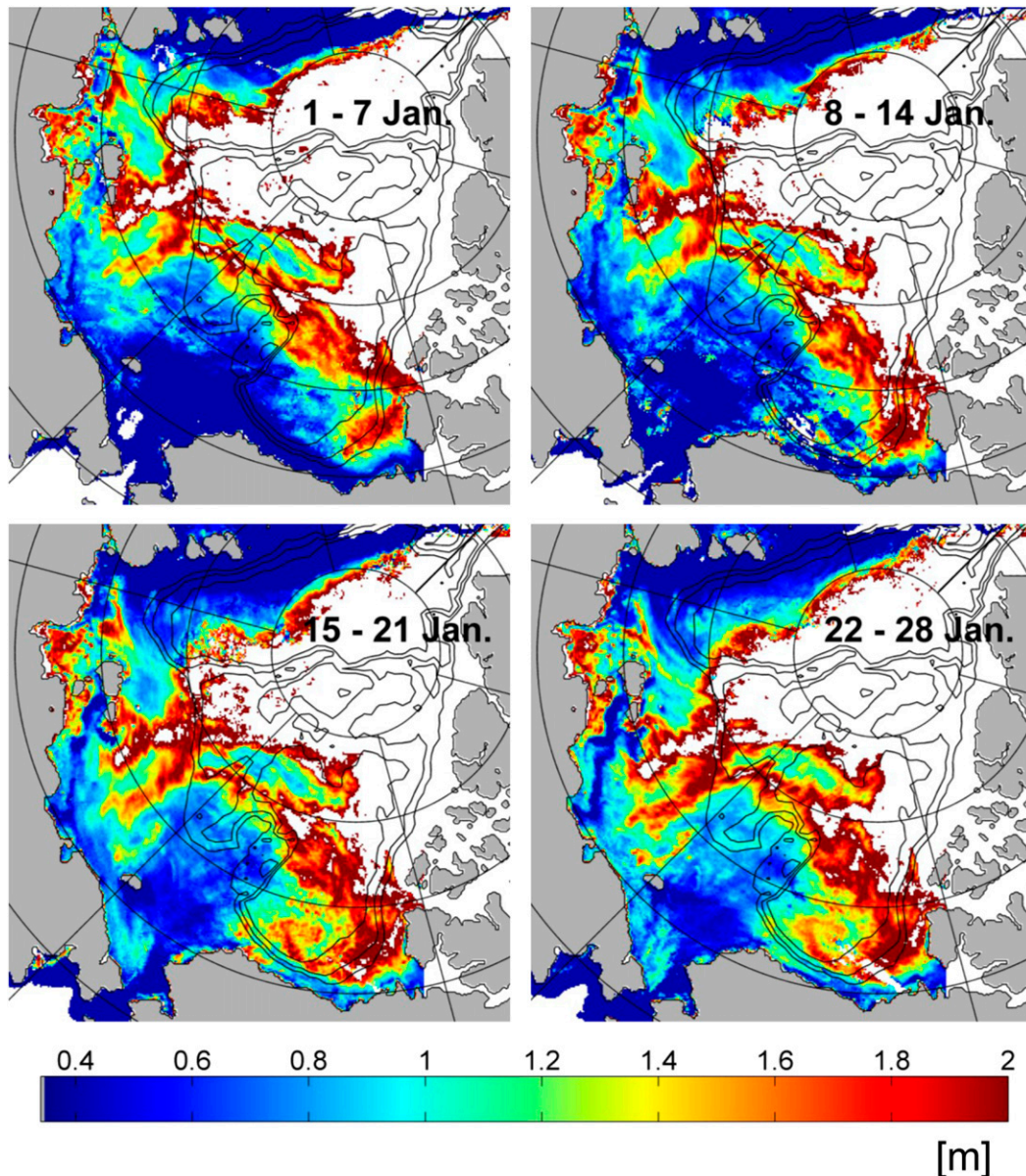


FIG. 12. Weekly averages of flat FYI draft estimated from Eq. (6) using filtered GR(18V, 36V) values for January 2017.

of sea surface salinity in the freeze-up period based on satellite measurements (e.g., Abe and Ebuchi 2014) will be useful for quality controls of mapped draft estimates.

From comparisons of the spectral gradient of brightness temperature data and in situ mode draft (Fig. 10b), a linear relationship between the two has been found for the earlier growth stage of FYI. The spectral gradients depending on flat sea ice draft, however, are expected to be obscure in the thicker FYI range because thermodynamic growth rates become small with increasing thickness. Indeed, the rates of declining emissivities at

frequencies above 18 GHz seem to decrease with increasing mode draft (Fig. 9). Therefore, to enhance the flat FYI thickness monitoring, it is important to examine how the present algorithm can be extended to the thick FYI range using further in situ observations covering the full range of thermodynamic FYI growth of ~ 2 m.

Although most MYI can survive through summer, whether FYI can survive through summer depends significantly on its thickness at melt onset and thus growth in the preceding freezing period. This suggests that in addition to summer climate conditions, FYI growth is a key

driver of summer sea ice variability in the present Arctic Ocean. Our algorithm improves FYI growth monitoring by providing precise draft estimates of flat ice in the earlier growth stage of FYI but underestimates rafted/ridged ice draft. Therefore, as a next step for further developments of the monitoring, it will be useful to estimate amplifications of the flat ice draft estimates as a result of rafting/ridging processes using high-precision sea ice velocity data.

Acknowledgments. Funding and data support to conduct this work were provided by the JAXA GCOM-W research project; the Green Network of Excellence (GRENE) Arctic Climate Change Research Project funded by the Ministry of Education, Culture, Sports, Science and Technology (MEXT), Japan; and the project titled “Korea-Arctic Ocean Observing System (K-AOOS), KOPRI, 20160245” funded by the Ministry of Oceans and Fisheries (MOF), South Korea. We greatly appreciate the efforts of Mr. Takeshi Wada in developing the algorithm. We thank the captains, officers, and crews of the CCGS *Louis S. St-Laurent* and the *ARAON* for their efforts in the deployment and recovery of the ocean mooring.

REFERENCES

- Abe, H., and N. Ebuchi, 2014: Evaluation of sea-surface salinity observed by Aquarius. *J. Geophys. Res. Oceans*, **119**, 8109–8121, <https://doi.org/10.1002/2014JC010094>.
- Cavalieri, D. J., 1994: A microwave technique for mapping thin sea ice. *J. Geophys. Res.*, **99**, 12 561–12 572, <https://doi.org/10.1029/94JC00707>.
- , P. Gloersen, and W. J. Campbell, 1984: Determination of sea ice parameters with the NIMBUS 7 SMMR. *J. Geophys. Res.*, **89**, 5355–5369, <https://doi.org/10.1029/JD089iD04p05355>.
- Comiso, J. C., 1983: Sea ice effective microwave emissivities from satellite passive microwave and infrared observations. *J. Geophys. Res.*, **88**, 7686–7704, <https://doi.org/10.1029/JC088iC12p07686>.
- , 2012: Large decadal decline of the Arctic multiyear ice cover. *J. Climate*, **25**, 1176–1193, <https://doi.org/10.1175/JCLI-D-11-00113.1>.
- , T. C. Grenfell, D. L. Bell, M. A. Lange, and S. F. Ackley, 1989: Passive microwave in situ observations of winter Weddell sea ice. *J. Geophys. Res.*, **94**, 10 891–10 905, <https://doi.org/10.1029/JC094iC08p10891>.
- Gloersen, P., and D. J. Cavalieri, 1986: Reduction of weather effects in the calculation of sea ice concentration from microwave radiance. *J. Geophys. Res.*, **91**, 3913–3919, <https://doi.org/10.1029/JC091iC03p03913>.
- Iwamoto, K., K. I. Ohshima, and T. Tamura, 2014: Improved mapping of sea ice production in the Arctic Ocean using AMSR-E thin ice thickness algorithm. *J. Geophys. Res. Oceans*, **119**, 3574–3594, <https://doi.org/10.1002/2013JC009749>.
- Kalnay, E., and Coauthors, 1996: The NCEP/NCAR 40-Year Reanalysis Project. *Bull. Amer. Meteor. Soc.*, **77**, 437–471, [https://doi.org/10.1175/1520-0477\(1996\)077<0437:TNYRP>2.0.CO;2](https://doi.org/10.1175/1520-0477(1996)077<0437:TNYRP>2.0.CO;2).
- Krishfield, R. A., A. Proshutinsky, K. Tateyama, W. J. Williams, E. C. Carmack, F. A. McLaughlin, and M.-L. Timmermans, 2014: Deterioration of perennial sea ice in the Beaufort Gyre from 2003 to 2012 and its impact on the oceanic freshwater cycle. *J. Geophys. Res. Oceans*, **119**, 1271–1305, <https://doi.org/10.1002/2013JC008999>.
- Kwok, R., 2006: Contrasts in sea ice deformation and production in the Arctic seasonal and perennial ice zones. *J. Geophys. Res.*, **111**, C11S22, <https://doi.org/10.1029/2005JC003246>.
- , G. F. Cunningham, M. Wensnahan, I. Rigor, H. J. Zwally, and D. Yi, 2009: Thinning and volume loss of the Arctic Ocean sea ice cover: 2003–2008. *J. Geophys. Res.*, **114**, C07005, <https://doi.org/10.1029/2009JC005312>.
- Laxon, S. W., and Coauthors, 2013: CryoSat-2 estimates of Arctic sea ice thickness and volume. *Geophys. Res. Lett.*, **40**, 732–737, <https://doi.org/10.1002/grl.50193>.
- Markus, T., and D. J. Cavalieri, 1998: Snow depth distribution over sea ice in the Southern Ocean from satellite passive microwave data. *Antarctic Sea Ice: Physical Processes, Interactions and Variability*, M. O. Jeffries, Ed., Antarctic Research Series, Vol. 74, Amer. Geophys. Union, 13–39.
- , J. C. Stroeve, and J. Miller, 2009: Recent changes in Arctic sea ice melt onset, freezeup, and melt season length. *J. Geophys. Res.*, **114**, C12024, <https://doi.org/10.1029/2009JC005436>.
- Martin, S., R. Drucker, R. Kwok, and B. Holt, 2004: Estimation of the thin ice thickness and heat flux for the Chukchi Sea Alaskan coast polynya from Special Sensor Microwave/Imager data, 1990–2001. *J. Geophys. Res.*, **109**, C10012, <https://doi.org/10.1029/2004JC002428>.
- Maslanik, J., J. Stroeve, C. Fowler, and W. Emery, 2011: Distribution and trends in Arctic sea ice age through spring 2011. *Geophys. Res. Lett.*, **38**, L13502, <https://doi.org/10.1029/2011GL047735>.
- Shimada, K., T. Kamoshida, M. Itoh, S. Nishino, E. Carmack, F. McLaughlin, S. Zimmermann, and A. Proshutinsky, 2006: Pacific Ocean inflow: Influence on catastrophic reduction of sea ice cover in the Arctic Ocean. *Geophys. Res. Lett.*, **33**, L08605, <https://doi.org/10.1029/2005GL025624>.
- Stroeve, J. C., T. Markus, L. Boisvert, J. Miller, and A. Barrett, 2014: Changes in Arctic melt season and implications for sea ice loss. *Geophys. Res. Lett.*, **41**, 1216–1225, <https://doi.org/10.1002/2013GL058951>.
- Tamura, T., and K. I. Ohshima, 2011: Mapping of sea ice production in the Arctic coastal polynyas. *J. Geophys. Res.*, **116**, C07030, <https://doi.org/10.1029/2010JC006586>.
- Tilling, R. L., A. Ridout, A. Shepherd, and D. J. Wingham, 2015: Increased Arctic sea ice volume after anomalously low melting in 2013. *Nat. Geosci.*, **8**, 643–646, <https://doi.org/10.1038/ngeo2489>.
- Yoshizawa, E., K. Shimada, H. K. Ha, T. W. Kim, S. H. Kang, and K. H. Chung, 2015: Delayed responses of the oceanic Beaufort Gyre to winds and sea ice motions: Influences on variations of sea ice cover in the Pacific sector of the Arctic Ocean. *J. Oceanogr.*, **71**, 187–197, <https://doi.org/10.1007/s10872-015-0276-6>.